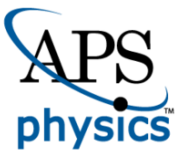

Nonequilibrium Scaling Behavior in Driven Soft Biological Assemblies

Federica Mura, Grzegorz Gradziuk, and Chase P. Broedersz

Phys. Rev. Lett. **121**, 038002 — Published 18 July 2018

DOI: 10.1103/PhysRevLett.121.038002

Non-equilibrium scaling behaviour in driven soft biological assemblies

Federica Mura,[1,*] Grzegorz Gradziuk,[1,*] and Chase P. Broedersz[1,†]

[1] *Arnold-Sommerfeld-Center for Theoretical Physics and Center for NanoScience, Ludwig-Maximilians-Universität München, D-80333 München, Germany.*

(Dated: April 13, 2018)

Measuring and quantifying non-equilibrium dynamics in active biological systems is a major challenge, because of their intrinsic stochastic nature and the limited number of variables accessible in any real experiment. We investigate what non-equilibrium information can be extracted from non-invasive measurements using a stochastic model of soft elastic networks with a heterogeneous distribution of activities, representing enzymatic force generation. In particular, we use this model to study how the non-equilibrium activity, detected by tracking two probes in the network, scales as a function of the distance between the probes. We quantify the non-equilibrium dynamics through the cycling frequencies, a simple measure of circulating currents in the phase space of the probes. We find that these cycling frequencies exhibit power-law scaling behavior with the distance between probes. In addition, we show that this scaling behavior governs the entropy production rate that can be recovered from the two traced probes. Our results provide insight in to how internal enzymatic driving generates non-equilibrium dynamics on different scales in soft biological assemblies.

Cells and tissue constitute a class of non-equilibrium many-body systems [1–5]. Indeed, non-equilibrium activity has been observed in various biological systems, including membranes [6, 7], chromosomes [8], and the cytoplasm [9–11]. A distinguishing physical feature of such biological assemblies is that they are driven out of equilibrium collectively by internal enzymatic processes that break detailed balance at the molecular scale. The active nature of living matter on larger scales can be determined non-invasively by observing the steady-state stochastic dynamics of mescoscopic degrees of freedom using time-lapse microscopy experiments: The non-equilibrium dynamics of these systems can manifest as circulating probability currents in a phase space of mesoscopic coordinates [2, 12–14]. However, it remains unclear how such non-equilibrium measures depend on the spatial scale on which the measurement is performed. A theoretical understanding of the spatial scaling behavior of broken detailed balance in internally driven biologically assemblies may reveal how to extract quantitative information from measurable phase space currents to characterize the active nature of the system.

Here we consider a simple, yet general model for an internally driven elastic assembly to study non-equilibrium scaling behavior. This assembly is driven out of equilibrium by heterogeneously distributed stochastic forces, representing internal enzymatic activity (Fig. 1). We quantify the non-equilibrium dynamics of such an assembly by the cycling frequencies associated to steady-state circulating currents in phase space [13, 14]. To study how broken detailed balance manifests on different scales in a given system, we investigate how the cycling frequency of a pair of tracer probes depends on the spatial distance between these probes. Interestingly, the cycling frequencies in our model exhibit a power-law scaling with the distance between probes with an exponent that depends on the dimensionality of the system. To provide a conceptual understanding of this scaling behavior, we develop an analytical calculation of these exponents. Furthermore, we show that the exponent associated to the power law of the cycling frequencies also underlies the scaling behavior of the entropy production rate that can be recovered from measured trajectories. Therefore, we provide a framework to study the spatial scaling behavior of non-equilibrium measures in soft elastic assemblies.

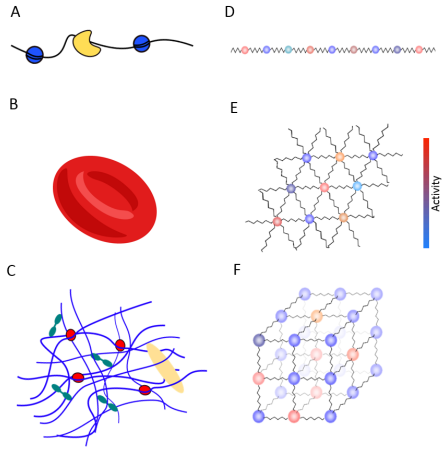

FIG. 1. Schematic illustrating soft viscoelastic networks with heterogeneous driving for various types of cellular systems. A) chromosome B) red blood cell membrane C) cytoskeletal network with in D-F associated bead-spring models with heterogeneous active driving. The color of the bead indicates the intensity of activity, representing the variance (increasing from blue to red) of the associated active noise process.

Our model consists of a d-dimensional elastic network of N beads, immersed in a simple Newtonian liquid at temperature T [15–18]. We assume a lattice structure where each bead is connected to its nearest neighbours by springs of elastic constant k, as illustrated in

Fig. 1. For simplicity, we model internal enzymatic activity by a Gaussian white noise with variance α_i at bead i. By assuming white noise, we effectively consider the dynamics of biological systems on time scales much longer than the characteristic timescales of the active processes [13, 19, 20]. Importantly, these activity amplitudes, $\alpha_i \geq 0$, are spatially heterogeneous, reflecting a spatial distribution of active processes in the system. These activity amplitudes are drawn independently from a distribution p_α with mean $\bar{\alpha} < \infty$ and standard deviation $\sigma_\alpha < \infty$ for each realization of the system. This description of a heterogeneously driven assembly is similar to bead-spring models in which the beads are coupled to distinct heat baths at different temperatures [21–23].

The temporal evolution of the probability distribution, $p(\mathbf{x}, t)$, of the beads' displacements $\mathbf{x}$, relative to their rest positions, is governed by a Fokker-Planck equation:

$$\begin{aligned} \frac{\partial p(\mathbf{x},t)}{\partial t} &= -\nabla \cdot [\mathbf{A}\mathbf{x} p(\mathbf{x},t)] + \nabla \cdot \mathbf{D} \nabla p(\mathbf{x},t), \\ &= -\nabla \cdot \mathbf{j}(\mathbf{x},t) \end{aligned} \tag{1}$$

where $\mathbf{j}(\mathbf{x}, t) = \mathbf{A}\mathbf{x}p(\mathbf{x}, t) - \mathbf{D}\nabla p(\mathbf{x}, t)$ is the probability current. Here, $\mathbf{A}$ is the elastic interaction matrix, incorporating all nearest neighbor spring interactions between beads; the mobility matrix is assumed to be diagonal to exclude hydrodynamic interactions between the beads, and is absorbed in $\mathbf{A}$. The diffusion matrix, $\mathbf{D}$, is diagonal with elements $d_{ij} = \delta_{ij}\frac{k_B(T+\alpha_i)}{\gamma}$, where γ is the damping coefficient describing the viscous interaction between a bead and the immersing liquid. The steady-state dynamics of this active network is described by

$$p(\mathbf{x}) = \frac{1}{\sqrt{(2\pi)^{dN} \det \mathbf{C}}} e^{-\frac{1}{2}\mathbf{x}^T \mathbf{C}^{-1} \mathbf{x}}, \tag{2}$$

where $\mathbf{C} = \langle \mathbf{x} \otimes \mathbf{x} \rangle$ is the covariance matrix, which can be obtained by solving the Lyapunov equation $\mathbf{AC} + \mathbf{CA}^T = -2\mathbf{D}$ [24]. In the simplest limit, the activities are spatially homogeneous: $\alpha_i = \alpha \ \forall i$, resulting in effectively equilibrium dynamics, with $p(\mathbf{x})$ given by the Boltzmann distribution ($\mathbf{C}^{-1} = -\mathbf{A}/(T + \alpha)$) and $\mathbf{j} = 0$. By contrast, in heterogeneously driven systems with non-identical α_i's, we obtain Non-Equilibrium Steady-State dynamics with $\mathbf{j} \neq 0$ [24].

If we were able to observe the stochastic motion of all beads in the network, we could directly measure the full probability current $\mathbf{j}(\mathbf{x})$ and extract information about the complete non-equilibrium dynamics of the system. However, in an actual experiment typically only a small subset of the degrees of freedom can be tracked (Fig. 2A). What information on the non-equilibrium dynamics of the system can be extracted from such limited observations? To address this question, we investigate a scenario where only a few degrees of freedom are accessible.

We start by reducing our description to the marginal distribution, $p_{\mathrm{r}}(\mathbf{x}_{\mathrm{r}}) = \int dx_{k \notin [r]} p(x_1, x_2, .., x_{dN})$, of a subset [r] of n tracked degrees of freedom $\mathbf{x}_{\mathrm{r}}$. By integrating out the subset [l] of m unobserved degrees of freedom $\mathbf{x}_{\mathrm{l}}$ on both sides of Eq. (1) and taking the steady-state limit, we obtain (see supplementary material):

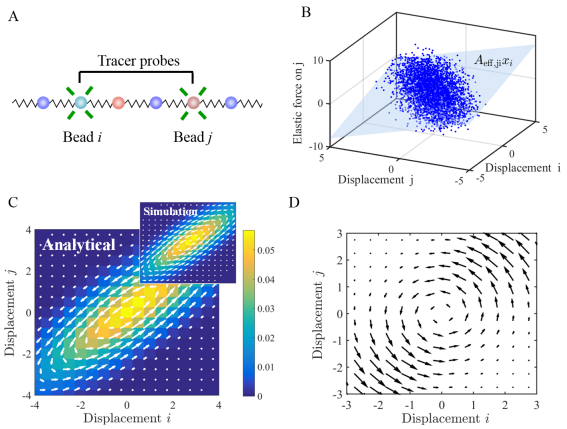

FIG. 2. Reduced system of tracked probed. A) Schematic of two fluorescently labelled probe beads in a larger system. B) Elastic force acting on bead j obtained at different time steps of a simulation of the Langevin dynamics of the full system (blue points), and the effective linear force, $\mathbf{A}_{\mathrm{eff}}\mathbf{x}_{\mathrm{r}}$, from analytical calculations (light blue plane). C) Probability density (color map) and probability current (white arrows) calculated analytically from the effective 2D system, together with results from simulating the full system in the inset. D) The non-conservative part of the effective force field: $\frac{(\mathbf{A}_{\mathrm{eff}} - \mathbf{A}_{\mathrm{eff}}^T)}{2}\mathbf{x}_{\mathrm{r}}$ (black arrows) can contribute to the rotation in phase space in non-equilibrium systems. Note, for $\alpha_i = \alpha \ \forall i$ (effective equilibrium scenario), $\mathbf{A}_{\mathrm{eff}}$ becomes symmetric.

$$0 = -\nabla \cdot [\mathbf{A}_{\mathrm{eff}}\mathbf{x}_{\mathrm{r}} p_{\mathrm{r}}(\mathbf{x}_{\mathrm{r}})] + \nabla \cdot \mathbf{D}_{[\mathrm{r,r}]} \nabla p_{\mathrm{r}}(\mathbf{x}_{\mathrm{r}}), \tag{3}$$

where the sub-index [r, r] of a matrix indicates the submatrix corresponding to the reduced set of observed variables. In addition, we introduce the effective linear interaction (Fig. 2B), which can be written as $\mathbf{A}_{\mathrm{eff}}\mathbf{x}_{\mathrm{r}}$, with $\mathbf{A}_{\mathrm{eff}} = \mathbf{A}_{[\mathrm{r,r}]} + \mathbf{A}_{[\mathrm{r,l}]}\mathbf{C}_{[\mathrm{l,r}]}\mathbf{C}^{-1}_{[\mathrm{r,r}]}$. Here, $\mathbf{A}_{[\mathrm{r,l}]}$ and $\mathbf{C}_{[\mathrm{l,r}]}$ are rectangular matrices of sizes $[n \times m]$ and $[m \times n]$, given by the elements of indices [r, l] of $\mathbf{A}$ and [l, r] of $\mathbf{C}$, respectively. Thus, we obtain an effective stationary Fokker-Planck equation for the reduced system (Eq. (3)). From this, we obtain the exact steady-state reduced probability distribution $p_{\mathrm{r}}(\mathbf{x}_{\mathrm{r}})$ and probability current density:

$$\mathbf{j}_{\mathrm{r}}(\mathbf{x}_{\mathrm{r}}) = \mathbf{A}_{\mathrm{eff}}\mathbf{x}_{\mathrm{r}} p_{\mathrm{r}}(\mathbf{x}_{\mathrm{r}}) + \mathbf{D}_{[\mathrm{r,r}]}\mathbf{C}^{-1}_{[\mathrm{r,r}]}\mathbf{x}_{\mathrm{r}} p_{\mathrm{r}}(\mathbf{x}_{\mathrm{r}}), \tag{4}$$

which can, in principle, be measured from the trajectories of the observed degrees of freedom (Fig. 2C).

We can use this reduced description to investigate how broken detailed balance manifests at different scales in the network. In particular, we consider the simplest case of a reduced system of only two tracked beads in a larger system, as illustrated in Fig. 2A. It is convenient to quantify the probability currents in the 2D phase space of

these two tracer beads by a pseudoscalar quantity: the average cycling frequency around the origin [13, 14, 25]. For linear systems, we can express the reduced probability current as $\mathbf{j}_{\mathrm{r}}(\mathbf{x}_{\mathrm{r}}) = \mathbf{\Omega}_{\mathrm{r}}\mathbf{x}_{\mathrm{r}}p_{\mathrm{r}}(\mathbf{x}_{\mathrm{r}})$, where $\mathbf{\Omega}_{\mathrm{r}}$ is a 2D matrix with purely imaginary eigenvalues $\lambda = \pm i\omega$, with ω representing the cycling frequency.

This cycling frequency can be measured experimentally for a pair of degrees of freedom, e.g. the displacements in a certain direction of two probe beads at a distance r. This frequency will depend on the specific configuration of all activity amplitudes α_i. We aim to compute how this cycling frequency depends on r after averaging over all activity configurations. Since ω is expected to be distributed symmetrically around 0, we calculate $\sqrt{\langle\omega^2(r)\rangle_\alpha}$ for pairs of beads separated by a distance r. Here, the average $\langle ...\rangle_\alpha$ is taken over an ensemble of activities $\{\alpha_i\}$ drawn from the distribution p_α. Intuitively, the magnitude of the circulation of currents in phase space typically decreases with the distance between the probes, as shown in Fig. 3A. This reduction of the circulation is reflected by a decrease of the cycling frequency ω with distance. Remarkably, $\sqrt{\langle\omega^2(r)\rangle_\alpha}$ appears to depend on the distance between the tracer beads, r, as a power law, $\sqrt{\langle\omega^2(r)\rangle_\alpha} \propto r^{-\mu}$, with $\mu \approx 1.9$ for a 1D chain with a folded Gaussian or an exponential distribution of activities, as depicted in Fig. 3B.

To investigate how the architecture of the system affects the scaling behavior of the cycling frequencies, we considered different network structures, including square, triangular, and cubic lattices. In particular, we determined the ensemble average $\langle..\rangle_\alpha$ by performing a spatial average for computational convenience (supplementary materials). Interestingly, we find that the characteristic exponent μ appears to depend strongly on the dimensionality of the lattice, but not on its geometry, as shown in Fig. 3B-C. These results suggest that the distance dependence of the cycling frequency is determined in part by the long wavelength elastic properties of the system. Importantly, however, the scaling of cycling frequency is sensitive to the spatial structure of the activities. For example, in the simple case of a delta-distributed (single-source) activity on a 1D chain, we find $\mu_{\mathrm{single}} \approx 2.4$ (Fig. 3B) in contrast to the value 1.9 obtained above for spatially distributed activities.

To obtain more insight into the scaling behavior of the cycling frequencies, we derive an analytical expression for the cycling frequency as a function of the distance between the observed beads, $\omega(r)$. In general, it can be shown that for a linear system described by a Fokker-Planck equation, the cycling frequencies are given by (supplementary materials):

$$\omega_{ij} = \frac{1}{2\gamma}\frac{\langle\tau_{ij}\rangle}{\sqrt{\det\mathbf{C}_{[\mathrm{r,r}]}}} \tag{5}$$

where $\tau_{ij} \coloneqq \mathbf{x}\times\mathbf{f}_{\mathrm{r}}(\mathbf{x}) = x_i f_j(\mathbf{x}) - x_j f_i(\mathbf{x})$ is a generalized phase space torque in the x_i-x_j plane, with $f_i(\mathbf{x})$ denoting the deterministic force acting on the i^{th} bead. This result is intuitive: for an overdamped system the mean angular velocity is proportional to the mean torque and the factor $1/\sqrt{\det\mathbf{C}_{[\mathrm{r,r}]}}$ ensures coordinate invariance. For the 1D chain of beads (Fig. 1D), Eq. (5) reduces to:

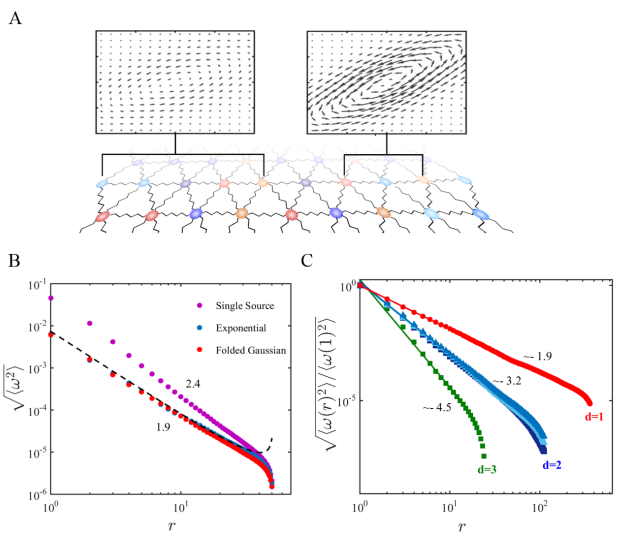

FIG. 3. Spatial scaling behavior of cycling frequencies. A) Steady-state current cycles in phase space of the displacements (along the lattice direction) of two tracer beads for a nearby pair of probes (left) and distant pair of probes (right). B) Scaling behavior of the cycling frequencies, $\sqrt{\langle\omega^2(r)\rangle}$, of a pair of probes beads as a function of their spatial distances, obtained for a 1D chain and different activity distributions, as indicated in the legend. C) Scaling behavior of the cycling frequencies, $\sqrt{\langle\omega^2(r)\rangle/\langle\omega^2(1)\rangle}$, obtained for different lattices and a folded Gaussian activity distribution. Triangular and square markers represent triangular and square/cubic lattices, respectively. Light/dark blue triangles represent triangular networks with zero/finite rest length springs. In both B) and C) we used $\bar{\alpha}/T = 0.15$

$$\omega_{ij} = \frac{k}{\gamma}\frac{\widetilde{\partial}_2^2 c_{ij}}{\sqrt{\det\mathbf{C}_{[\mathrm{r,r}]}}}, \tag{6}$$

where c_{ij} is the i,j^{th} element of the covariance matrix $\mathbf{C}$, and with the discrete second derivative across rows denoted as: $\widetilde{\partial}_2^2 c_{ij} = c_{i,j+1} - 2c_{i,j} + c_{i,j-1}$. Thereby, we have reduced the problem of calculating $\omega(r)$ to finding the covariance matrix of the system.

The structure of $\mathbf{D}$ suggests a natural decomposition of the covariance matrix $\mathbf{C}$ into equilibrium ($\overline{\mathbf{C}}$) and non-equilibrium ($\mathbf{C}^*$) contributions: $\mathbf{C} = (k_BT/k)\overline{\mathbf{C}} + (k_B\bar{\alpha}/k)\mathbf{C}^*$, such that $\overline{\mathbf{C}}$ and $\mathbf{C}^*$ are dimensionless. Both $\overline{\mathbf{C}}$ and $\mathbf{C}^*$ can be found by solving the Lyapunov equation, which for the 1D chain is given by

$$\widetilde{\partial}_1^2\bar{c}_{ij} + \widetilde{\partial}_2^2\bar{c}_{ij} = -2\delta_{ij} \tag{7}$$

$$\widetilde{\partial}_1^2 c^*_{ij} + \widetilde{\partial}_2^2 c^*_{ij} = -2\delta_{ij}\frac{\alpha_i}{\bar{\alpha}}, \tag{8}$$

where $\widetilde{\partial}_1^2$ indicates the discrete second derivative across columns. These equations represent discrete stationary diffusion equations, with sources of divergence given by δ_{ij} and $\delta_{ij}(\alpha_i/\bar{\alpha})$, respectively. This result prescribes how a spatial distribution of activities structures the covariance matrix.

We can make further progress by noting that the principle of detailed balance imposes $\omega_{ij} = 0$ at thermal equilibrium, which together with Eq. (6) implies $\widetilde{\partial}_2^2 \bar{c}_{ij} = 0$. We can, therefore, substitute $\widetilde{\partial}_2^2 c_{ij}$ in Eq.(6) by $\widetilde{\partial}_2^2 c^*_{ij}$, and then expand this equation up to linear order in $\bar{\alpha}/T$ to obtain

$$\omega_{ij} = \frac{k}{\gamma}\frac{\bar{\alpha}}{T}\frac{\widetilde{\partial}_2^2 c^*_{ij}}{\sqrt{\det \overline{\mathbf{C}}_{[\mathrm{r,r}]}}}. \tag{9}$$

We proceed by calculating $\mathbf{C}^*$ for a given distribution of activities $\{\alpha_i\}$. Because of the linearity of Eq. (8), $\mathbf{C}^*$ is a superposition of steady-state solutions to single-source problem, i.e. a delta-distribution for which all but one of the activities would be set to zero. Denoting the element of $\mathbf{C}^*$ at a distance r from the single activity source by $c^*(r)$, we obtain the "covariance current" $\partial_r c^*(r) \sim 1/r$. Here we employed a continuous approximation of the discrete diffusion problem in Eqs. (7) and (8). Thus, $c^*(r) = -a\ln(r) + b$ for a single-source problem with integration constants a and b, representing the Green's function for our problem. Using this expression for $c^*(r)$ together with Eq. (9), we obtain for the single source case: $\omega^2_{\mathrm{single}}(r) = \frac{k^2}{\gamma^2}\frac{\alpha^2}{T^2}\frac{a^2}{r^4}\frac{1}{\det \overline{\mathbf{C}}_{[\mathrm{r,r}]}(r)}$, where α is the source's activity.

Next, we use a superposition of single source solutions for $c^*(r)$ to obtain the non-equilibrium contribution of the covariance matrix $\mathbf{C}^*$ for a specific configuration of many activity sources $\{\alpha_i\}$. Using this result in conjunction with Eq. (9) and performing an ensemble average over the distribution of activity realizations, we arrive at the central result

$$\langle \omega^2(r)\rangle_\alpha = \frac{k^2}{\gamma^2}\frac{\sigma_\alpha^2}{T^2}\frac{\pi a^2}{2r^3}\frac{1}{\det \overline{\mathbf{C}}_{[\mathrm{r,r}]}(r)}. \tag{10}$$

Finally, we note that the elements of the equilibrium covariance matrix are given by $\bar{c}_{i,j} = \min(i,j) - ij/(N+1)$, and find that for $r \ll N$, $\det \overline{\mathbf{C}}_{[\mathrm{r,r}]}(r)$ exhibits a power law behavior, $\det \overline{\mathbf{C}}_{[\mathrm{r,r}]}(r) \sim Nr$. Therefore, from this analysis we find for a 1D chain with heterogenous activities $\mu = 2$, independent of the activity distribution p_α. Furthermore, we find $\mu_{\mathrm{single}} = 2.5$ for a single-source activity, in accord with our numerical result (see Fig.3B). This calculation provides insight into how a combination of features of the equilibrium and non-equilibrium contributions to the covariance matrix determine the spatial scaling behavior of cycling frequencies.

Non-zero cycling frequencies directly reflect broken detailed balance, suggesting a connection between ω and

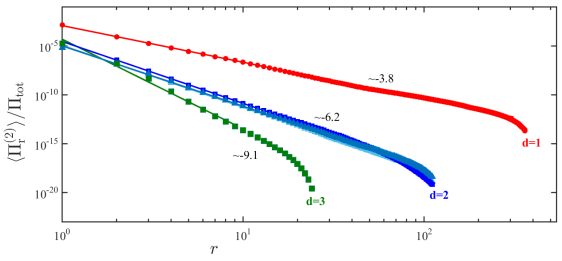

FIG. 4. Spatial scaling behavior of the average entropy production rate, $\langle \Pi_{\mathrm{r}}^{(2)}\rangle$, of a pair of probe beads as a function of their spatial distance r, obtained for different lattices and a folded Gaussian activity distribution with $\bar{\alpha}/T = 0.15$. Note the entropy production rate of the reduced system is scaled by the total entropy production rate of the whole network, Π_{tot}. Triangular and square markers represent triangular and square/cubic lattices, respectively. Light/dark blue triangles represent triangular networks with zero/finite rest length springs.

measures of the internal driving, including the rate of entropy production. For a Markovian system described by a Fokker-Planck equation, the total entropy production rate under steady-state conditions is given by [26]:

$$\Pi_{\mathrm{tot}} = k_{\mathrm{B}} \int d\mathbf{x} \frac{\mathbf{j}^T(\mathbf{x})\mathbf{D}^{-1}\mathbf{j}(\mathbf{x})}{p(\mathbf{x})}, \tag{11}$$

where k_{B} is Boltzmann's constant. The validity of this result relies on the equivalence between the Fokker-Planck and Langevin descriptions. However, the marginal probability density of the reduced system is described by a Fokker-Planck equation only at steady-state (see Eq. (3) and supplementary materials), reflecting the loss of Markovianity after coarse-graining. Even if the real dynamics of the reduced system are non-Markovian, we can define an effective Markovian dynamics through the Langevin equation

$$\frac{d\mathbf{x}_{\mathrm{r}}(t)}{dt} = \mathbf{A}_{\mathrm{eff}}\mathbf{x}_{\mathrm{r}}(t) + \sqrt{2\mathbf{D}_{[\mathrm{r,r}]}}\,\xi_{\mathrm{r}}(t), \tag{12}$$

with Gaussian white noise $\xi_{\mathrm{r}}(t)$. This equation of motion results in the exact steady-state probability and current densities, but with an approximate stochastic dynamics. In particular, the effective interaction matrix $\mathbf{A}_{\mathrm{eff}}$ (see Eq. (3)) captures only the average interaction between the traced variables, as illustrated in Fig. 2B. Furthermore, in contrast to the full deterministic forces ($\mathbf{Ax}$), these effective interactions (Fig. 2C) need not to derive from a potential and, thus, may contain a non-conservative component (Fig. 2D).

The entropy production rate associated with the effective Markovian dynamics in Eq.(12) is given by

$$\Pi_{\mathrm{r}} = k_B \int d\mathbf{x}_{\mathrm{r}} \frac{\mathbf{j}_{\mathrm{r}}^T(\mathbf{x}_{\mathrm{r}})\mathbf{D}^{-1}_{[\mathrm{r,r}]}\mathbf{j}_{\mathrm{r}}(\mathbf{x}_{\mathrm{r}})}{p_{\mathrm{r}}(\mathbf{x}_{\mathrm{r}})} \leq \Pi_{\mathrm{tot}}, \tag{13}$$

where $\mathbf{j}_{\mathrm{r}}(\mathbf{x}_{\mathrm{r}})$ is defined in Eq. (4). Note, estimating Π_{r} by using the Markovian formalism allows us to set a lower bound for the total entropy production rate Π_{tot} (supplementary materials), similar to what already shown for discrete systems [27]. In the $n = 2$ case with two traced degrees of freedom that we consider here, Eq. (13) reduces to (supplementary materials)

$$\Pi_{\mathrm{r}}^{(2)} = k_B\omega^2 \,\mathrm{Tr}\,(\mathbf{C}_{[\mathrm{r},\mathrm{r}]}\mathbf{D}_{[\mathrm{r},\mathrm{r}]}^{-1}). \tag{14}$$

This result provides an explicit relation between the partial entropy production rate and the cycling frequency ω. Note, all quantities in the expression for $\Pi_{\mathrm{r}}^{(2)}$ can be observed in an experiment, providing a direct way to non-invasively determine the reduced rate of entropy production for a set of traced degrees of freedom. Since $\mathrm{Tr}\,(\mathbf{C}_{[\mathrm{r},\mathrm{r}]}\mathbf{D}_{[\mathrm{r},\mathrm{r}]}^{-1})$ depends only weakly on r, as long as $1 \ll r \ll N$, we expect a scaling behavior $\langle\Pi_{\mathrm{r}}^{(2)}\rangle \sim r^{-2\mu}$. This result shows that the spatial scaling behavior of the cycling frequencies directly determines the spatial scaling behavior of the entropy production rate.

In summary, we here demonstrate theoretically how experimental measures of non-equilibrium activity in internally driven linear networks are affected by the length-scale at which the system is observed. Specifically, we developed a general framework to predict the scaling behavior of cycling frequencies and the entropy production rate that can be inferred by tracing pairs of degrees of freedom. We showed the exponent μ that governs this behavior for a system with heterogeneous random activities, is insensitive to the details of distribution of activities. However, this exponent depends sensitively on the dimensionality of the system. The predicted scaling behaviour can be tested, for instance, by analyzing the fluctuations of pairs of tracer particles embedded in biological [9–11, 28, 29] and artifical [30–35] systems under non-equilibrium steady-state conditions.

We thank S. Ceolin, E. Frey, J. Gladrow, F. Gnesotto, P. Ronceray, and C. Schmidt for stimulating discussions. This work was supported by the German Excellence Initiative via the program NanoSystems Initiative Munich (NIM), by a DFG Fellowship through the Graduate School of Quantitative Biosciences Munich (QBM). Part of this work was performed at the Aspen Center for Physics supported by NSF grant PHY-1607611.

* These authors contributed equally
† C.broedersz@lmu.de

[1] Fodor E., Marchetti M. C. ArXiv **1708** 08652, (2017).
[2] F. Gnesotto, F. Mura, J. Gladrow, C. P. Broedersz Rep. Prog. Phys. (in press)
[3] F. Jülicher, K. Kruse, J. Prost, J.-F. Joanny Physics Reports **449** 1, (2007).
[4] D. Needleman, Z. Dogic Nat. Rev. Mater **2**, (2017).
[5] C. F. Schmidt, and F. C. MacKintosh Curr. Opin. Cell Biol. 22, 29 (2010).
[6] T. Betz, M. Lenz, J. F. Joanny, C. Sykes, Proc. Natl. Acad. Sci. **36**, 106 (2009).
[7] H. Turlier, D. A. Fedosov, B. Audoly, T. Auth, N. S. Gov, J. -F. Joanny, G. Gompper, T. Betz Nature Physics **12**, 513-519 (2016).
[8] S. C. Weber, A. J. Spakowitz, J. A. Theriot, Proc. Natl. Acad. Sci. **19**, 109 (2010).
[9] A. W. C. Lau, B. D. Hoffman, A. Davies, J. C. Crocker, T. C. Lubensky Phys. Rev. Lett. **19**, 91 (2003).
[10] M. Guo, A. J. Ehrlicher, M. H. Jensen, M. Renz, J. R. Moore, R. D. Goldman, J. L. Schwartz, F. C. Mackintosh, D. A. Weitz Cell **4**, 158 (2014).
[11] N. Fakhri, A. D. Wessel, C. Willms, M. Pasquali, D. R. Klopfenstein, F. C. Mackintosh, C. F. Schmidt Science **6187**, 344 (2014).
[12] C. Battle, C. P. Broedersz, N. Fakhri, J. Howard, C. F. Schmidt, F. C. MacKintosh Science **6285**, 352 (2016).
[13] J. Gladrow, N. Fakhri, F. C. MacKintosh, C. F. Schmidt, C. P. Broedersz, Phys. Rev. Lett. **24**, 116 (2016).
[14] J. Gladrow, C. P. Broedersz, C. F. Schmidt Phys. Rev. E **2**, 96 (2017).
[15] M. G. Yucht, M. Sheinman, C. P. Broedersz, Soft Matter, **9** (29) (2013).
[16] C. P. Broedersz, F. C. MacKintosh Rev. Mod. Phys, **86** (3) (2014).
[17] D. Osmanovic, Y. Rabin, Soft Matter, 13, 963 (2017).
[18] X. Mao, T. C. Lubensky Annu. Rev. Condens. Matter Phys, **9** (0) (2018).
[19] F. C. MacKintosh, A. J. Levine Phys. Rev. Lett, **100** (1) 018104 (2008).
[20] J. Ruostekoski, J. R. Anglin Phys. Rev. Lett, **91** (19) 190402 (2003).
[21] Z. Rieder, J. L. Lebowitz, E.Lieb J. Math. Phys **8** 1073 (1967).
[22] F. Bonetto, J. L. Lebowitz, J. Lukkarinen J. Stat. Phys **116** (2004).
[23] G. Falasco, M. Baiesi, L. Molinaro, L. Conti, F. Baldovin Phys. Rev. E **92** 022129 (2015).
[24] H. Risken, Springer, Berlin, Heidelberg, 1996.
[25] J. B. Weiss, Tellus A **3**, 55 (2003).
[26] U. Seifert, Reports Prog. Phys. **12**, 75 (2012).
[27] G. Bisker, M. Polettini, T. R. Gingrich, J. M. Horowitz J. Stat. Mech. Theory Exp **2017** 093210 (2017).
[28] D. Mizuno, C. Tardin, C. F. Schmidt, F. C. MacKintosh Science **5810**, 315 (2007).
[29] A. D. Wessel, M. Gumalla, J. Grosshans, C. F. Schmidt Biophys. J., 108, 1899 (2015)
[30] O. Lieleg, M. M. A. E. Claessens, A. R. Bauch Soft Matter, **6** (2) (2010).
[31] J. Palacci, S. Sacanna, A. P. Steinberg, D. J. Pine, P. M. Chaikin, Science, 1230020 (2013).
[32] I. Buttinoni, J. Bialké, F. Kümmel, H. Löwen, C. Bechinger, T. Speck, Phys. Rev. Lett., 110(23), (2013).
[33] G. H. Koenderink, Z. Dogic, F. Nakamura, P. M. Bendix, F. C. MacKintosh, j. H. Hartwig, T. P. Stossel, D. A. Weitz, Proc. Natl. Acad. Sci., **106**, 36. (2009)
[34] M. H. Jensen, E. J. Morris, D. A. Weitz Biochim. Biophys, **1853** (11 0 0) (2015).
[35] V. Schaller, C. Weber, C. Semmrich, E. Frey, A. R. Bausch, Nature, 467, 7311 (2010)
[36] Y. L. Tong, Springer Series in Statistics, Springer-Verlag, 1990.

Appendices

DERIVATION OF EQ. (3)

Here, we derive Eq. (3), which describes the steady state distribution of traced variables. Integrating out the unobserved degrees of freedom on both sides of the Fokker-Plank equation (Eq. (1)), and using the Einstein notation for summing over repeated indexes, we obtain:

$$\overbrace{\int d\mathbf{x}_\mathrm{l}\partial_t p(\mathbf{x})}^{(I)} = -\overbrace{\int d\mathbf{x}_\mathrm{l}\partial_i[a_{ij}x_j p(\mathbf{x},t)]}^{(II)} + \overbrace{\int d\mathbf{x}_\mathrm{l} d_{ij}\partial_i\partial_j p(\mathbf{x},t)}^{(III)} \tag{15}$$

where a_{ij} and d_{ij} are the elements of the interaction matrix $\mathbf{A}$ and the diffusion matrix $\mathbf{D}$, respectively. Rewriting the probability as $p(\mathbf{x},t) = p(\mathbf{x}_\mathrm{l}|\mathbf{x}_\mathrm{r},t)p_\mathrm{r}(\mathbf{x}_\mathrm{r},t)$, we can separately calculate each term in Eq.(15). The first term (I) gives:

$$\int d\mathbf{x}_\mathrm{l}\partial_t p_\mathrm{r}(\mathbf{x}_\mathrm{r},t)p(\mathbf{x}_\mathrm{l}|\mathbf{x}_\mathrm{r},t) = \partial_t p_\mathrm{r}(\mathbf{x}_\mathrm{r},t)\int d\mathbf{x}_\mathrm{l} p(\mathbf{x}_\mathrm{l}|\mathbf{x}_\mathrm{r},t) = \partial_t p_\mathrm{r}(\mathbf{x}_\mathrm{r},t) \tag{16}$$

For the second term (II), we obtain

$$\begin{aligned}\int d\mathbf{x}_\mathrm{l}\partial_i[p_\mathrm{r}(\mathbf{x}_\mathrm{r},t)p(\mathbf{x}_\mathrm{l}|\mathbf{x}_\mathrm{r},t)a_{ij}x_j] &= \delta_{i,[\mathrm{r}]}\partial_i[p_\mathrm{r}(\mathbf{x}_\mathrm{r},t)\int d\mathbf{x}_\mathrm{l} p(\mathbf{x}_\mathrm{l}|\mathbf{x}_\mathrm{r},t)a_{ij}x_j] \\ &= \delta_{i,[\mathrm{r}]}\partial_i[p_\mathrm{r}(\mathbf{x}_\mathrm{r},t)a_{ij}\left\langle x_j|\mathbf{x}_\mathrm{r},t\right\rangle]\end{aligned} \tag{17}$$

where $\delta_{i,[\mathrm{r}]} = 1$ if x_i is one of the observed coordinates and zero otherwise. In the first line we use that the probability density vanishes at infinity faster than $1/x$. Similarly, the third term (III) can be written as

$$\begin{aligned}\int d\mathbf{x}_\mathrm{l} d_{ij}\partial_i\partial_j[p_\mathrm{r}(\mathbf{x}_\mathrm{r},t)p(\mathbf{x}_\mathrm{l}|\mathbf{x}_\mathrm{r},t)] &= \delta_{i,[\mathrm{r}]}\delta_{j,[\mathrm{r}]}d_{ij}\partial_i\partial_j[p_\mathrm{r}(\mathbf{x}_\mathrm{r},t)\int d\mathbf{x}_\mathrm{l} p(\mathbf{x}_\mathrm{l}|\mathbf{x}_\mathrm{r},t)] \\ &= \delta_{i,[\mathrm{r}]}\delta_{j,[\mathrm{r}]}d_{ij}\partial_i\partial_j p_\mathrm{r}(\mathbf{x}_\mathrm{r},t)\end{aligned} \tag{18}$$

We seek a description for the stochastic dynamics, which only depends on the observed degrees of freedom. This can be achieved by taking the steady-state limit. In this case, the conditional average appearing in Eq.(17) yields $\langle\mathbf{x}_\mathrm{l}|\mathbf{x}_\mathrm{r}\rangle = \mathbf{C}_{[\mathrm{l,r}]}\mathbf{C}^{-1}_{[\mathrm{r,r}]}\mathbf{x}_\mathrm{r}$ [36]. We substitute Eqs. (16)-(18) in Eq. (15) to obtain Eq. (3), which therefore holds only at steady-state.

DERIVATION OF EQ. (5)

Here we derive the expression in Eq. (5) for the cycling frequencies. To this end, we first show that the right hand side of this equation is invariant under orientation preserving linear transformations restricted to the 2-dimensional reduced subspace. Let us consider such a transformation: $\mathbf{x}'_\mathrm{r} = \mathbf{B}\mathbf{x}_\mathrm{r}$, $\mathbf{f}'_\mathrm{r} = \mathbf{B}\mathbf{f}_\mathrm{r}$, and denote by $\mathbf{C}'_{[\mathrm{r,r}]}$ the reduced covariance matrix in the transformed coordinates.

$$\mathbf{B}\mathbf{C}_{[\mathrm{r,r}]}\mathbf{B}^T = \mathbf{C}'_{[\mathrm{r,r}]} \quad\Longrightarrow\quad \det\mathbf{B} = \sqrt{\frac{\det\mathbf{C}'_{[\mathrm{r,r}]}}{\det\mathbf{C}_{[\mathrm{r,r}]}}} \tag{19}$$

Using this result together with the transformation properties of the vector product, we obtain

$$\frac{\langle\tau_{ij}\rangle}{\sqrt{\det\mathbf{C}_{[\mathrm{r,r}]}}} = \frac{\langle\mathbf{x}_\mathrm{r}\times\mathbf{f}_\mathrm{r}(\mathbf{x})\rangle}{\sqrt{\det\mathbf{C}_{[\mathrm{r,r}]}}} = \frac{\langle\mathbf{x}'_\mathrm{r}\times\mathbf{f}'_\mathrm{r}(\mathbf{x}')\rangle}{\sqrt{\det\mathbf{C}_{[\mathrm{r,r}]}}}\frac{1}{\det\mathbf{B}} = \frac{\langle\tau'_{ij}\rangle}{\sqrt{\det\mathbf{C}'_{[\mathrm{r,r}]}}}. \tag{20}$$

The coordinate invariance of this term allows us to specifically consider the convenient coordinates in which $\mathbf{C}_{[\mathrm{r,r}]} = \mathbf{I}$:

$$\frac{1}{\gamma}\langle\tau_{ij}\rangle = \frac{1}{\gamma}\langle\mathbf{x}_\mathrm{r}\times\mathbf{f}_\mathrm{r}(\mathbf{x})\rangle = \frac{1}{\gamma}\int d\mathbf{x}_\mathrm{r}\,\langle\mathbf{x}_\mathrm{r}\times\mathbf{f}_\mathrm{r}(\mathbf{x})|\mathbf{x}_\mathrm{r}\rangle\,p_\mathrm{r}(\mathbf{x}_\mathrm{r}) = \frac{1}{\gamma}\int d\mathbf{x}_\mathrm{r}\;\mathbf{x}_\mathrm{r}\times\langle\mathbf{f}_\mathrm{r}(\mathbf{x})|\mathbf{x}_\mathrm{r}\rangle\,p_\mathrm{r}(\mathbf{x}_\mathrm{r}) \tag{21}$$

We can further expand this expression by using $\mathbf{\Omega}_{\rm r} = \mathbf{A}_{\rm eff} + \mathbf{D}_{[{\rm r},{\rm r}]}\mathbf{C}^{-1}_{[{\rm r},{\rm r}]}$. (The expression for $\mathbf{\Omega}_{\rm r}$ follows immediately from Eq. (4), since we require $\mathbf{j}_{\rm r}(\mathbf{x}_{\rm r}) = \mathbf{\Omega}_{\rm r}\mathbf{x}_{\rm r}p_{\rm r}(\mathbf{x}_{\rm r})$.)

$$\frac{1}{\gamma}\langle \mathbf{f}_{\rm r}(\mathbf{x})|\mathbf{x}_{\rm r}\rangle = \mathbf{A}_{\rm eff}\mathbf{x}_{\rm r} = \mathbf{\Omega}_{\rm r}\mathbf{x}_{\rm r} - \mathbf{D}_{[{\rm r},{\rm r}]}\mathbf{C}^{-1}_{[{\rm r},{\rm r}]}\mathbf{x}_{\rm r}. \tag{22}$$

Combining this result with Eq. (21), we arrive at

$$\frac{1}{\gamma}\langle \tau_{ij}\rangle = \int d\mathbf{x}_{\rm r}\ \mathbf{x}_{\rm r}\times(\mathbf{\Omega}_{\rm r}\mathbf{x}_{\rm r})p_{\rm r}(\mathbf{x}_{\rm r}) - \int d\mathbf{x}_{\rm r}\ \mathbf{x}_{\rm r}\times(\mathbf{D}_{[{\rm r},{\rm r}]}\mathbf{C}^{-1}_{[{\rm r},{\rm r}]}\mathbf{x}_{\rm r})p_{\rm r}(\mathbf{x}_{\rm r}). \tag{23}$$

Using the explicit form of $\mathbf{\Omega}_{\rm r}$ (see Eq. (31)), we evaluate the first term in this expression,

$$\int d\mathbf{x}_{\rm r}\ \mathbf{x}_{\rm r}\times(\mathbf{\Omega}_{\rm r}\mathbf{x}_{\rm r})p_{\rm r}(\mathbf{x}_{\rm r}) = \int d\mathbf{x}_{\rm r}\ \omega_{ij}(x_i^2+x_j^2)p_{\rm r}(\mathbf{x}_{\rm r}) = \omega_{ij}(c_{ii}+c_{jj}) = 2\omega_{ij}. \tag{24}$$

In addition, we confirm by direct calculation, that, as expected, the second term in Eq. (23) vanishes:

$$-\int d\mathbf{x}_{\rm r}\ \mathbf{x}_{\rm r}\times(\mathbf{D}_{[{\rm r},{\rm r}]}\mathbf{x}_{\rm r})p_{\rm r}(\mathbf{x}_{\rm r}) = \int d\mathbf{x}_{\rm r}\ (-x_j,\ x_i)\begin{pmatrix} d_{ii} & d_{ij}\\ d_{ij} & d_{jj}\end{pmatrix}\begin{pmatrix}x_i\\ x_j\end{pmatrix}p_{\rm r}(\mathbf{x}_{\rm r}) = \tag{25}$$

$$= \int d\mathbf{x}_{\rm r}\ [-d_{ii}x_ix_j - d_{ij}x_j^2 + d_{ij}x_i^2 + d_{jj}x_ix_j]p_{\rm r}(\mathbf{x}_{\rm r}) = \tag{26}$$

$$= \underbrace{c_{ij}}_{0}(d_{jj}-d_{ii}) + d_{ij}\underbrace{(c_{ii}-c_{jj})}_{0} = 0 \tag{27}$$

Altogether, this gives us the desired result:

$$\frac{1}{2\gamma}\frac{\langle\tau_{ij}\rangle}{\sqrt{\det\mathbf{C}_{[{\rm r},{\rm r}]}}} = \omega_{ij} \tag{28}$$

DERIVATION OF EQ.13

Here we show that $\Pi_{\rm tot} \geq \Pi_{\rm rr}$.

$$\begin{aligned}\frac{\Pi_{\rm tot}-\Pi_{\rm r}}{k_{\rm B}} &= \int d\mathbf{x}\frac{\mathbf{j}^T(\mathbf{x})\mathbf{D}^{-1}\mathbf{j}(\mathbf{x})}{p(\mathbf{x})} - \int d\mathbf{x}_{\rm r}\frac{\mathbf{j}_{\rm r}^T(\mathbf{x}_{\rm r})\mathbf{D}^{-1}_{[{\rm r},{\rm r}]}\mathbf{j}_{\rm r}(\mathbf{x}_{\rm r})}{p(\mathbf{x}_{\rm r})}\\ &= \frac{\gamma}{k_{\rm B}}\sum_{j\in[l]}\int d\mathbf{x}\frac{v_j^2(\mathbf{x})}{(T+\alpha_j)}p(\mathbf{x}) + \frac{\gamma}{k_{\rm B}}\sum_{i\in[r]}\left[\left(\int d\mathbf{x}\frac{v_i^2(\mathbf{x})}{(T+\alpha_i)}p(\mathbf{x})\right) - \int d\mathbf{x}_{\rm r}\frac{\langle v_i(\mathbf{x})|\mathbf{x}_{\rm r}\rangle^2}{(T+\alpha_i)}p(\mathbf{x}_{\rm r})\right]\\ &= \frac{\gamma}{k_{\rm B}}\left[\sum_{j\in[l]}\int d\mathbf{x}\frac{v_j^2(\mathbf{x})}{(T+\alpha_j)}p(\mathbf{x}) + \sum_{i\in[r]}\int d\mathbf{x}_{\rm r}\left[\left(\int d\mathbf{x}_{\rm l}\frac{v_i^2(\mathbf{x})}{(T+\alpha_i)}p(\mathbf{x}_{\rm l}|\mathbf{x}_{\rm r})p(\mathbf{x}_{\rm r})\right) - \frac{\langle v_i(\mathbf{x})|\mathbf{x}_{\rm r}\rangle^2}{(T+\alpha_i)}p(\mathbf{x}_{\rm r})\right]\right]\\ &= \frac{\gamma}{k_{\rm B}}\left[\sum_{j\in[l]}\frac{\langle v_j^2(\mathbf{x})\rangle}{(T+\alpha_j)} + \sum_{i\in[r]}\int d\mathbf{x}_{\rm r}\underbrace{\left(\langle v_i^2(\mathbf{x})|\mathbf{x}_{\rm r}\rangle - \langle v_i(\mathbf{x})|\mathbf{x}_{\rm r}\rangle^2\right)}_{\geq 0}\frac{p(\mathbf{x}_{\rm r})}{(T+\alpha_i)}\right] \geq 0\end{aligned} \tag{29}$$

where in the second line we use that $\mathbf{D}$ is diagonal, $\mathbf{v}(\mathbf{x}) = \mathbf{j}(\mathbf{x})/p(\mathbf{x})$, and $\mathbf{j}_{\rm r}(\mathbf{x}_{\rm r}) = p(\mathbf{x}_{\rm r})\int d\mathbf{x}_{\rm l}\ \mathbf{v}_{\rm r}(\mathbf{x})p(\mathbf{x}_{\rm l}|\mathbf{x}_{\rm r}) = p(\mathbf{x}_{\rm r})\langle\mathbf{v}_{\rm r}(\mathbf{x})|\mathbf{x}_{\rm r}\rangle$, which follows from the derivation of Eq. (3).

DERIVATION OF EQ. (14)

Here we derive the expression for the partial entropy production rate in terms of the cycling frequencies (see Eq.(14)). It is convenient to substitute the current field $\mathbf{j} = \mathbf{\Omega}\mathbf{x}p(\mathbf{x})$ in Eq. (11), which gives

$$\begin{aligned}\Pi &= k_{\rm B}\int d\mathbf{x}(\mathbf{\Omega}\mathbf{x})^T\mathbf{D}^{-1}(\mathbf{\Omega}\mathbf{x})p(\mathbf{x}) = k_{\rm B}\int d\mathbf{x}\, x_i\Omega_{ij}^T(\mathbf{D}^{-1})_{jl}\Omega_{lm}x_mp(\mathbf{x})\\ &= k_{\rm B}\Omega_{ij}^T(\mathbf{D}^{-1})_{jl}\Omega_{lm}c_{mi} = k_{\rm B}\,{\rm Tr}\,(\mathbf{\Omega}^T\mathbf{D}^{-1}\mathbf{\Omega}\mathbf{C}).\end{aligned} \tag{30}$$

Since the entropy production is invariant under coordinate transformations, we can use a more suitable coordinate system. In particular, we choose a set of coordinates such that $\mathbf{C} = \mathbb{1}$. In this set of coordinates, the entries of the matrix Ω_{ij} correspond to the cycling frequencies in the coordinates space of the i^{th} and j^{th} coordinates [25]. Thus, in the 2D case $\mathbf{\Omega}_{\mathrm{r}}$ is given by

$$\mathbf{\Omega}_{\mathrm{r}} = \begin{pmatrix} 0 & \omega \\ -\omega & 0 \end{pmatrix} \tag{31}$$

Furthermore, in this coordinate system $\mathbf{C}_{[\mathrm{r,r}]}$ and $\mathbf{\Omega}_{\mathrm{r}}$ commute, yielding

$$\Pi_{\mathrm{r}}^{(2)} = k_B \omega^2 \,\mathrm{Tr}\,(\mathbf{C}_{[\mathrm{r,r}]}\mathbf{D}_{[\mathrm{r,r}]}^{-1}) \tag{32}$$

Note, this expression is invariant under coordinate transformations.

SYSTEM SIZE AND SPATIAL AVERAGE

We determined the scaling of cycling frequencies for a range of system sizes (Fig. 5A). By properly rescaling both axes (see Eq.(10)), we can collapse all data on a mastercurve, which is consistent with a power-law over at least two decades (Fig. 5B). This analysis suggests a universal behavior, which is not dependent on the size of the system. These results provides additional numerical evidence for a power law scaling.

To determine ensemble averages of the cycling frequencies in Fig.(3) and Fig.(4) we employ spatial averages. For an infinite heterogeneous system, the ensemble average is equivalent to a spatial average. In a finite system, we need to be careful when using spatial averages because of edge effects. We investigated this aspect in a 1D chain, for which edge effects will be stronger than in higher dimensional systems. We performed a spatial average over all the different beads at distance r in the system, where we excluded data from beads at distances < 10 from the edge of system. Using this procedure, we find results that are consistent with those obtained with the ensemble average. (Fig. 6)

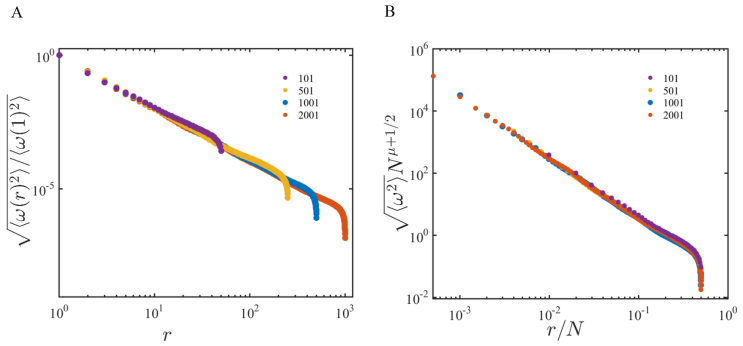

FIG. 5. Spatial scaling behavior of cycling frequencies. A) Scaling behavior of the frequency for different system sizes in the 1D chain (other parameters as in Fig. 3). B) Data collapse obtained by properly rescaling both axes.

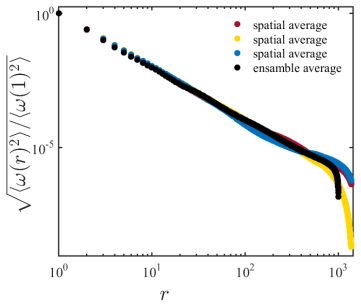

FIG. 6. Comparison between spatial and ensemble averages of the cycling frequencies for a 1D chain of size N=1501 (other parameters as in Fig. 3).